Multi-omics reveal critical differentiation target for Parkinson's Disease-vulnerable midbrain dopaminergic neurons

Author Information

Roberto Garcia-Swinburn[1*#], Guochang Lyu[1,3#], Judith C. Kreutzmann[1,2] , Anqi Xiong[1], Rika Kojima[2], Carmen Abaurre[1], Chiara Tremolanti[1], Sandra Gellhaar[1], Per Uhlén[1], Per Svenningsonn[2,4], Gonçalo Castelo-Branco[1], Carmen Salto[1], Onur Dagliyan[1*], Ernest Arenas[1,3†]

Affiliations

[1]Laboratory of Molecular Neurobiology, Department of Medical Biochemistry and Biophysics, Karolinska Institutet, 171 77 Stockholm, Sweden

[2]Department of Clinical Neuroscience, Karolinska Institutet, 171 76 Stockholm, Sweden

[3]Aligning Science Across Parkinson's (ASAP) Collaborative Research Network, Chevy Chase, MD, 20815.

[4]Department of Basic and Clinical Neuroscience, King's College London, WC2R 2LS London, UK

*Corresponding author: roberto.garcia.swinburn@ki.se or onur.dagliyan@ki.se

[#]These authors contributed equally

† Deceased 15/09/2024

Abstract

Parkinson's disease (PD) is characterized by the progressive loss of midbrain dopaminergic (mDA) neurons, leading to severe debilitating motor impairment. Recent single-cell analyses have revealed that specific mDA subpopulations, such as SOX6$^+$ AGTR1$^+$ neurons, are most vulnerable to degeneration. Current human pluripotent stem cell differentiation protocols fail to selectively generate these subtypes. Here we describe a multiomic-guided strategy that enriches SOX6$^+$ mDA neurons by combining enhancing Sonic Hedgehog agonism with prolonged Wnt activation. This approach accelerates floor plate specification, increases expression of mDA developmental

markers, and increases substantially the yield of SOX6$^+$ mature mDA neurons compared to prior attempts. Following intrastriatal transplantation into hemiparkinsonian mice, these cells restore motor function in approximately 4 months and generated grafts containing SOX6$^+$ A9-like neurons. Our work thus establishes a reproducible differentiation platform for generating the PD-susceptible mDA subtype, providing a foundation for precision disease modelling and subtype-targeted cell replacement therapies.

Introduction

Parkinson's disease (PD), the second most prevalent neurodegenerative disorder, lacks curative treatments, severely impacting patients' quality of life. This condition is characterized by the progressive degeneration of midbrain dopaminergic (mDA) neurons in the substantia nigra pars compacta (SNpc). The loss of these neurons, which project primarily to the dorsal striatum, depletes dopaminergic input and leads to the characteristic motor symptoms of PD[1]. Although advances in pharmacological therapies have been made, these treatments are often insufficient in halting disease progression or restoring lost neuronal function in later stages[2]. Cell therapy offers a promising alternative, with the potential to replace the damaged or lost DA neurons critical to PD pathology[3].

Advances in stem cell and midbrain development research have enabled the generation of transplantable mDA progenitors from human pluripotent stem cells (hPSCs)[4–7]. Success in preclinical models has led to the development of clinical-grade mDA progenitors for PD clinical trials[8–11] with recent phase I/II clinical trials reporting safe outcomes, thereby paving the way for future medical use of hPSCs[12,13].

However, the translational promise of hPSC-derived cell therapies hinges on the precise composition and quality of the grafted cells. Single-cell transcriptomic studies have begun to molecularly define the diversity of human mDA neurons[14,15], both in development and in hPSC-derived midbrain cultures[7,15–17]. These studies have revealed a critical challenge: not all mDA neurons are equally susceptible to PD. Recent work has reported complications like dyskinesias, which is linked to serotonergic neuron contamination in fetal transplants[18]. Thus, the inability of existing differentiation protocols, which generate heterogeneous mixes of mDA subtypes, to specifically target this critical population represents a significant limitation for both disease modelling and the development of precision cell therapies.

Single-cell transcriptomics has revealed significant diversity within mDA neurons in the adult human SNpc, categorizing them into three major subtypes based on the expression of *SOX6*, *CALB1*, and *GAD2*, establishing that the SOX6 subpopulation is the most susceptible to degeneration[19,20]. These subtypes emerge during human mDA neuron development[14], and recent single-cell epigenomic profiling (e.g., ATAC-seq) further elucidates midbrain differentiation[21]. To generate PD-vulnerable SOX6$^+$ mDA neurons, we first developed a simplified differentiation protocol based on recently identified key developmental regulators[7], but molecular phenotyping revealed unstable phenotypes at later stages, indicating insufficient patterning. This prompted reviewing multiomic data leading to implement two key protocol modifications: enhanced ventralization via stronger Sonic Hedgehog (SHH) pathway agonization and prolonged Wnt activation improved midbrain patterning, with elevated *OTX2*, *EN1* and *SOX6* expression in engineered cells. Transplanting these engineered cells into hemiparkinsonian (hemiPD) rodent models demonstrated their therapeutic efficacy, yielding grafts enriched with SOX6$^+$ mDA neurons and restoring motor function. Thus, we here report a multiomic-guided differentiation

strategy that specifically enriches for the critical PD-vulnerable mDA subtype and validates its therapeutic potential *in vivo*.

Results

Longitudinal multiomic single-nuclei sequencing delineates the cell-type composition throughout the process of midbrain dopaminergic neuron differentiation *in vitro*

Building upon our recently published method[22], we designed a new protocol focused on precise midbrain floor plate (mFP) patterning and improving cell viability to generate sufficient progenitor cells, while expanding compatibility to a broader range of human induced pluripotent stem cell lines. Our protocol enabled sequential differentiation of human induced pluripotent stem cells (hiPSCs) into midbrain progenitors, positive in mFP progenitor markers such as FOXA2, OTX2 and LMX1A, and functional neurons expressing canonical mDA markers like CORIN, TH or Nurr1 (Fig. 1a, Extended Fig. 1).

To delineate developmental trajectories, we performed single-cell multiomic sequencing (scATAC-seq + scRNAseq) in benchmarked wild-type iPSCs (KOLF2.1J) at five developmental stages (Days *in vitro* (DIV): DIV11, 16, 28, 42 and 56; Fig. 1b). Following quality control and filtering, we annotated 9,233 high-quality nuclei using integrated manual-automatic classification based on cluster-specific markers and developing human brain references[14] categorized into major types, with sequential differentiation to a mature DA identity based on their enriched GO terms (Fig. 1c,d). Chronologically, early stages (DIV11-16) showed high expression of regional specification markers (LMX1A, OTX2). By DIV28, dopaminergic commitment marker NR4A2 upregulated, while late stages (DIV42-56) exhibited elevated expression of maturation markers

94 (such as TH, NR4A2, KCNJ6), indicating functional specification (Fig. 1e, Extended Fig. 2).
95 Further chromatin accessibility analysis showed precursor cell types such as floor plate progenitors
96 (ProgFP), medial neuroblasts (NbM) and DA clusters to recapitulate expected chromatin access
97 (*SOX6* and *LMX1A* for mDA progenitors, and *DDC* for mature functional mDA neurons) with
98 ProgFP having a higher potential to differentiate to SOX6 populations (Fig. 1g). We then validated
99 our annotations by comparing them to publicly available scRNA-seq datasets from human fetal
100 midbrain samples[14], by quantifying cell type identity across individual cells. As a result, our
101 annotated cell types closely resembled their endogenous counterparts, as demonstrated by
102 hierarchical clustering (Fig. 1f). High similarity scores (>0.8) were predominantly observed during
103 early stages of the midbrain differentiation and were primarily enriched in ProgFP and NbM,
104 underscoring the effectiveness of our approach in recapitulating endogenous early mDA neuron
105 development. Radial glia cell subtypes, Rgl2 and Rgl3, also displayed transcriptomic profiles akin
106 to their counterparts *in vivo*, hinting at the establishment of an mDA signaling niche to deliver cell
107 type-specific developmental factors for neuronal maturation *in vitro*[23]. At advanced stages, mDA
108 neurons, closely matched their endogenous cells from reference datasets (reference DA and DA0
109 vs experimental DA similarity score >0.8). These findings show that while mDA neurons matched
110 reference profiles, later stages may benefit from extended maturation cues to enhance postmitotic
111 neuronal survival.

112 Reconstructed differentiation trajectory resolves transcriptional dynamics during 113 mDA lineage specification and maturation

114 To move beyond chronological staging and define the molecular logic of *in vitro* differentiation,
115 we reconstructed the developmental trajectory of the dopaminergic lineage. We isolated

116 progenitor and neuronal populations (ProgFP, NbM and mDA neurons) from our multiomic
117 dataset and inferred their relationships using pseudotime ordering and RNA velocity. Both
118 analyses confirmed a direct progression from ProgFP and NbM progenitors to mature mDA
119 neurons, validating the protocol's ability to recapitulate this fundamental lineage path (Fig. 1h).
120 Uniform manifold approximation and projection (UMAP) analysis revealed a continuous
121 maturation trajectory for mDA neurons. Gene Ontology (GO) analysis of genes ordered along this
122 path showed a developmentally-relevant progression of biological processes: initial neurite
123 outgrowth was followed by neurotransmitter release, synaptic assembly, and finally synaptic
124 modulation (Extended Fig. 2b), matching the pattern observed in pseudotime analysis.
125 Intriguingly, we observed heterogeneity in the maturation routes. Intriguingly, we observed
126 heterogeneity in the maturation routes. While most cells followed the canonical path, a subset of
127 late-stage cells (DIV42–56) appeared to bypass the axonal development phase characteristic of
128 DIV28, suggesting the existence of alternative maturation mechanisms, potentially influenced by
129 laminar identity cues established earlier in development[24].
130 We next applied single-cell regulatory network inference and clustering (SCENIC) to identify
131 stage-specific regulons. Clustering of AUCell scores for activities of each regulon revealed distinct
132 segregation between early neural progenitors, ProgFP, and NbM, and their descendant mDA
133 neurons along the development trajectory (Fig. 1i). We identified key transcription factors (TFs)
134 orchestrating each developmental transition. In ProgFP cells, the NR3C1 (glucocorticoid receptor)
135 regulon was upregulated, promoting progenitor pool expansion by skewing cells toward
136 proliferation over differentiation[25]. Concurrently, SREBF1, a pro-neural transcription factor
137 controlling mDA neurogenesis[26], activity drove the subsequent transition to neurogenic
138 progenitors (NProg). In NbM cells, pro-neural TFs NEUROD1 and NHLH1 emerged as top

139 regulons, initiating neurogenesis and differentiation in postmitotic cells[27,28]. Subtypes of mDA
140 neurons shared a core set of transcription factors, including PBX1, a canonical regulator of mDA
141 specification and survival[29]. In contrast, transcription factors as POU2F2 and BCL11A displayed
142 more specialized roles at distinct maturation stages[17,30]. In conclusion, trajectory reconstruction
143 confirms that our differentiation protocol recapitulates key embryological processes of mDA
144 development. More importantly, this approach provides a powerful *de novo* framework for
145 identifying the developmental regulatory modules, offering deeper insights into dopaminergic
146 neuron differentiation and maturation.

147 An iterative enhancement in ventralization improves floorplate patterning and 148 accelerates neuronal conversion

149 Given that robust regional patterning underpins high-quality mDA neuron generation, and our
150 single-cell data suggested suboptimal ventralization, we hypothesized that enhanced ventralization
151 would improve patterning outcomes. We induced Engrailed 1 (EN1), a well-established marker
152 for mDA neuron specification[36], while streamlining the protocol for scalability. EN1 plays a
153 pivotal role from the earliest stages of regional specification and maintenance of mDA neurons in
154 adulthood[31]. It supports the midbrain-hindbrain boundary formation during development and
155 sustains mDA function by regulating key genes (*TH, VMAT2, DAT,* and *ALDH1A1*) in postmitotic
156 neurons[31,32]. Thus, EN1 serves as both a surrogate for enhanced mDA neuron specification quality
157 and a predictor of transplantation outcome[9].
158 To enhance EN1 expression, we applied a higher concentration of the SHH agonist
159 purmorphamine[6], and optimized culture conditions to maintain cell viability (Fig. 2a).
160 Subsequently, elevated purmorphamine significantly boosted EN1 expression at DIV11

161 (Optimized: 88.53% ± 6.8%; Original: 20.00% ± 3.65%) without altering core floor plate markers
162 FOXA2 or LMX1A (Fig.2b,e; Extended Fig.3a). The effects of this enhanced ventralization were
163 more pronounced at later stages. By DIV16, during the fate transition from NbM towards early
164 mDA neurons, new protocol cultures exhibited an accelerated TH^+ neuron generation (Optimized:
165 26.12% ± 3.93%; Original: 3.57% ± 1.68%) and increased co-expression of TH^+, $EN1^+$ and
166 $SOX6^+$ (Optimized: 75.92% ± 1.26%; Original: 7.56% ± 5.11%; Fig. 2c,f). This improved
167 molecular signature persisted through maturation (DIV28), with sustained co-expression of EN1
168 and SOX6 (Optimized: 65.44% ± 7.06%; Original: 5.35% ± 3.75%; Fig. 2d,g, Extended Fig. 3b).
169 These neurons exhibited functional maturity, displaying calcium dynamics characteristic of mDA
170 neurons by DIV42 (Fig. 2h). Furthermore, we applied this differentiation protocol to GBA^{E236K}
171 hiPSC NH50143 and isogenic corrected cells NH50142, which showed similar enhancements in
172 EN1 expression and DA marker progression (Extended Fig. 4).
173 To molecularly characterize the improvements driven by enhanced ventralization, we performed
174 single-nuclei RNA sequencing (snRNA-seq) on cells from the new protocol at DIV14,16 and 28.
175 The new protocol accelerated differentiation, with a higher proportion of NProg and NbM
176 emerging at earlier stages, accompanied by a reduction in ProgFP cells (Fig. 3b). Using the same
177 annotation methods as in the previous dataset, the resulting mDA lineage cell types were enriched
178 with classic mDA neuron marker genes (Fig. 3c), including *FOXA2, LMX1A, OTX2, TH,* and
179 *NR4A2*, and showed an expected developmental trajectory across different cell populations (Fig.
180 3d). Critically, postmitotic cells exhibited higher EN1, sustained OTX2 and SOX6, and elevated
181 maturation markers TH, SLC18A2 (VMAT2), and CALB1[33] (Fig. 3f).
182 SCENIC analysis identified the key transcription factors activated by the new protocol (Fig. 3e).
183 The paired-box transcription factor PAX7 transiently became the dominant regulon in NProg,

184 suggesting precise rostro-caudal patterning as it contributes to determine the midbrain-hindbrain
185 boundary during regionalization[34,35]. Other leading regulons in NProg and NbM cells are also
186 actively involved in guiding the neuronal identity acquisition. For instance, POU3F1 and ZEB1
187 are essential regulators of neural lineage commitment, often working synergistically to coordinate
188 correct orders of neuronal development, as POU3F1 promotes early neural fate decisions, while
189 ZEB1 modulates the developmental timing and prevents premature differentiation[36,37]. Notably,
190 PITX3 emerged as a leading regulon in mDA neurons, which reflects the progressive acquisition
191 of mature mDA phenotypes[38] and highlights their molecular similarity to endogenous SNpc mDA
192 neurons (Fig. 3e,f). Regulon activity profiles from the integrated dataset revealed a distinct and
193 significant regulatory impacts of TCF4 and TCF12 under the new protocol (Extended Fig. 5c).
194 Interestingly, the new protocol also appeared to enhance SREBF1 expression throughout
195 differentiation, linking it to its known role in regulating midbrain dopaminergic neurogenesis[26],
196 and its involvement in controlling neuronal dendrite expansion through lipid homeostasis[39].
197 Overall, a targeted intervention to enhance ventralization, guided by multiomic insight, profoundly
198 accelerated and improved the specification of mDA neurons, driving them toward a transcriptomic
199 profile that closely resembles that of endogenous, vulnerable SNpc neurons.

200 Transplanted hiPSC-derived neurons mature into striatum-innervating dopaminergic 201 neurons and restore motor function in hemiPD mice

202 Having established that our optimized protocol enriches ventralized mDA subpopulation *in vitro*,
203 we next evaluated the therapeutic potential of our engineered cells *in vivo* using hemiparkinsonian
204 rodent models.. We unilaterally lesioned immunocompromised B6RGS mice by injecting 6-
205 OHDA into the medial forebrain bundle (MFB). Upon confirming hemiparkinsonism, we

206 intrastriatally transplanted 200,000 cells into randomly selected mice. Motor recovery was
207 assessed longitudinally by amphetamine-induced ipsilateral rotations, showing that grafted
208 hemiPD animals returned to pre-lesion state 4 months post-implant (m.p.i.), which was maintained
209 1 month later, ending our grafting experiment (Sham: -0.24 ± 0.73; 6-OHDA: 13.41 ± 1.43;
210 Grafted: -0.70 ±1.18 net ipsilateral rotations/min). To ensure overall motor recovery, we also
211 analysed complex motor coordination by tape removal test (Sham: -0.40 ± 0.34; 6-OHDA: 19.51
212 ± 2.50; Grafted: -2.82 ±0.96 net ipsilateral removal time) and pole test (Sham: 5.00 ± 0.59; 6-
213 OHDA: 21.25 ± 3.53; Grafted: 8.56 ± 1.13 seconds), and spontaneous motor activity by cylinder
214 wall test (Sham: 51.82 ± 3.73%; 6-OHDA: 8.85 ± 4.75%; Grafted: 40.89 ± 3.73% ipsilateral
215 contacts). Human cells were detected in these 5-month grafts by STEM121^{+} staining, confirming
216 that grafted cells did not migrate to other regions (Fig. 4c). Furthermore, human DANs were
217 detected by double positive staining of TH and HuNu, with these cells showing extended
218 processes, characteristic of mDA neurons (Fig. 4d,e). Using stereological quantification of
219 TH^{+}/HuNu^{+} cells (Fig. 4F), grafts were estimated to have 160000 human nuclei (155700 ± 35893),
220 of which about 10% were also stained positively for TH (10.36 ± 0.73%). Additionally, no actively
221 proliferative human cells were found within the grafts (Extended Fig. 6)
222 After establishing the presence of DANs within our grafts, we aimed to analyse if these DANs
223 recapitulated the phenotypical aspects of the most PD-vulnerable portion of nigral DANs which
224 have been reported to be A9-subtype (DANs from the SNpc), more specifically the
225 SOX6^{+}/AGTR1a^{+} subpopulation located in the ventral SNpc[19,40]. To this aim, we performed a
226 series of IHC analysis of the grafted DANs. A majority of grafted TH^{+} cells were found to be
227 positive for several markers distinctive to the PD-vulnerable A9-subtype (Fig 4g,h), such as SOX6
228 (84.67 ± 3.03%), ALDH1A1 (50.67 ± 2.37%) and AGTR1 (64.16 ± 4.97%). In contrast, a minority

229 of the DANS stained positively for the A10-subtype marker Calbindin (29.92 ± 3.45%). Another
230 aspect that we wanted to evaluate is the expression of canonical markers for mDA neurons in the
231 grafted TH^+ cells (Fig. 4i,j). We performed IHC and we identified approximately all of the grafted
232 DANs as $LMX1A^+$ (92.09 ± 3.37%), $FOXA2^+$ (96.66 ± 1.88%), $NR4A2^+$ (96.19 ± 2.16%) and
233 $PITX3^+$ (85.14 ± 1.80%). Finally, we performed another series of IHC to evaluate expression of
234 proteins involved in DA regulation and secretion (Fig. 4k,l). We were able to determine that the
235 grafted DANs expressed DAT (90.03 ± 1.23%), GIRK2 (96.78 ± 2.12%), VMAT (94.24 ± 1.47%)
236 and DDC (100.00 ± 0.00%). Overall, these results show that grafted cells mature into a large
237 percentage of DANs expressing canonical markers for A9-subtype mDA neurons that are able to
238 ameliorate motor degeneration in rodent PD models.

239 snRNA-seq reveals A9-subtype mDA neuron enrichment in grafts

240 To unbiasedly characterize graft compositionand transcriptional fidelity to the transplanted
241 neurons to native human neuron subtypes, we performed snRNA-seq on graft tissue from three
242 transplanted mice. After quality control, we retained 9196 high-quality human nuclei.
243 Unsupervised clustering revealed that the graft composition consisted of four main cell lineages:
244 neurons, radial glia, gliobasts and oligodendroglial lineage cells, with no presence of vascular
245 leptomeningeal meningeal cells (VLMC) contamination, an off-target population in mDA neuron
246 differentiation[41] (Fig. 5a, Extended Fig. 7). Further analysis of the neuronal clusters (defined by
247 RBFOX3) resolved into four distinct populations: dopaminergic (DAergic), glutamatergic,
248 GABAergic ,and a small cluster of neural progenitors (defined by high expression of INA)
249 (Extended Fig. 8a, Extended Fig. 9a).
250 Critically, the DAergic cluster was comprised of 3 distinct subclusters: DA_SOX6, DA_CALB1
251 and DA_ONECUT2 (Fig. 5b). DA clusters exhibited high expression of canonical dopaminergic

252 markers (*TH, DDC, NR4A2, LMX1A, PBX1, SLC18A2* [VMAT2], *SLC6A3* [DAT], *PITX3, KCNJ6*
253 [GIRK2]), whereas GABA and glutamatergic clusters lacked these but expressed *GAD1* and *GAD2*
254 and *SLC17A6* [VGLUT2], respectively. INA clusters were distinguished from glutamatergic
255 clusters by elevated *SLC17A6*, *STMN2* and *INA* expression (Extended Fig. 8b,c, Extended Fig.
256 9b,c) . Within the DA lineage, subclusters were resolved by differential expression of SOX6,
257 CALB1 and ONECUT2 (Fig. 5c,d). Roughly half of DA cells were classified as DA_SOX6 (44.73
258 ± 4.79%), with the remainder predominantly DA_CALB1 and a minority DA_ONECUT2 (Fig.
259 5e). These results confirm our protocol's capacity to produce PD-susceptible $SOX6^+$ mDA subtype
260 *in vivo*.

261 Transcriptomic comparison validates fidelity of grafted neurons to native human 262 midbrain subtypes

263 To rigorously benchmark the identity of our grafted dopaminergic neurons, we compared their
264 transcriptional profiles directly to those of native adult human mDA cells. We performed a
265 MetaNeighbor analysis, a quantitative method for assessing cell type similarity, comparing our
266 graft-derived DA subclusters to the well-annotated dopaminergic subtypes from a reference single
267 cell atlas of the human substantia nigra[19] (Fig. 5f). This analysis showed high distinctive
268 resemblance with a score >0.8 between our DA_SOX6 subcluster and the SOX6_AGTR1
269 subcluster from Kamath dataset, which have been reported to be the most susceptible
270 subpopulation to PD[19,40]. In contrast, the DA_ONECUT2 subcluster showed resemblance to the
271 human CALB1_TRHR reported to be the most resilient. However, the DA_CALB1 subcluster
272 lacked exclusive alignment with any Kamath cluster, instead showing broad similarity to multiple
273 $CALB1^+$ subtypes, indicating incomplete subtype commitment or ongoing differentiation in this

274 population. These results confirm successful *in vivo* differentiation into SOX6$^+$ mDA neurons
275 mirroring PD-vulnerable human counterparts reinforces that we were successfully able to generate
276 cells that differentiate *in vivo* to cells resembling human SOX6 mDA neurons.

277 Gene regulatory network analysis confirms stable commitment of SOX6$^+$ 278 dopaminergic neurons

279 Given the transcriptional similarity of grafted DA neurons to native human subtypes, we assessed
280 whether SOX6$^+$ subtype represented a stably committed fate or a transitional state. GO analysis
281 revealed distinct functional specializations among the dopaminergic subclusters, consistent with
282 advanced maturation (Fig. 5g). The DA_SOX6 population was enriched for terms related to
283 synaptic transmission and organization, hallmarks of functional, integrated neurons. In contrast,
284 the DA_CALB1 and DA_ONECUT2 clusters were associated with terms like "learning" and
285 "regulation of cell projection," suggesting nuanced, subtype-specific functional roles. (Fig. 5g).
286 To directly infer developmental potential, we performed RNA velocity analysis on our DA and
287 immature neurons subclusters. We found that immature neurons have the potential to become
288 DA_CALB1 cells. Interestingly, the DA_CALB1 subclusters have the potential to become either
289 DA_ONECUT2 or DA_SOX6, which in contrast their velocity show that these identities were a
290 stable endpoint, not a transient phase (Fig. 5h, Extended Fig. 9d,e, Extended Fig. 10).
291 Further evaluation of the gene regulatory network by SCENIC established that the DA clusters
292 were enriched in exclusive TFs expression profile, not found in the immature neuron, GABA or
293 Glut clusters (Fig. 5i, Extended Fig. 9f). For example, PBX1 regulon networks have been
294 associated with ventral midbrain DA organization and is highly enriched (score >0.8) in our DA
295 cluster. Moreover, the DA_SOX6 is differentially highly enriched in SOX6 (score >0.8) and
296 CUX2 (score >0.6) within the DA clusters. Interestingly, the CUX2 regulon network has been

297 reported to be highly associated with the $SOX6^{+}AGTR1^{+}$ clusters of neurons in human datasets,
298 further validated in PD macaque models[19,42]. In conclusion, this multi-faceted computational
299 analysis demonstrates that our grafts contain mature, synaptically active neurons whose subtype
300 identities are locked in by stable gene regulatory networks. The DA_SOX6 population, in
301 particular, represents a terminal, committed fate, confirming that our protocol generates the
302 precise, stable, and vulnerable neuronal subtype required for accurate disease modeling and
303 effective cell therapy for PD.
304

Fig. 1: Single nuclei multi-omic sequencing revealed the diversity of cellular composition during mDA neuron differentiation *in vitro*.

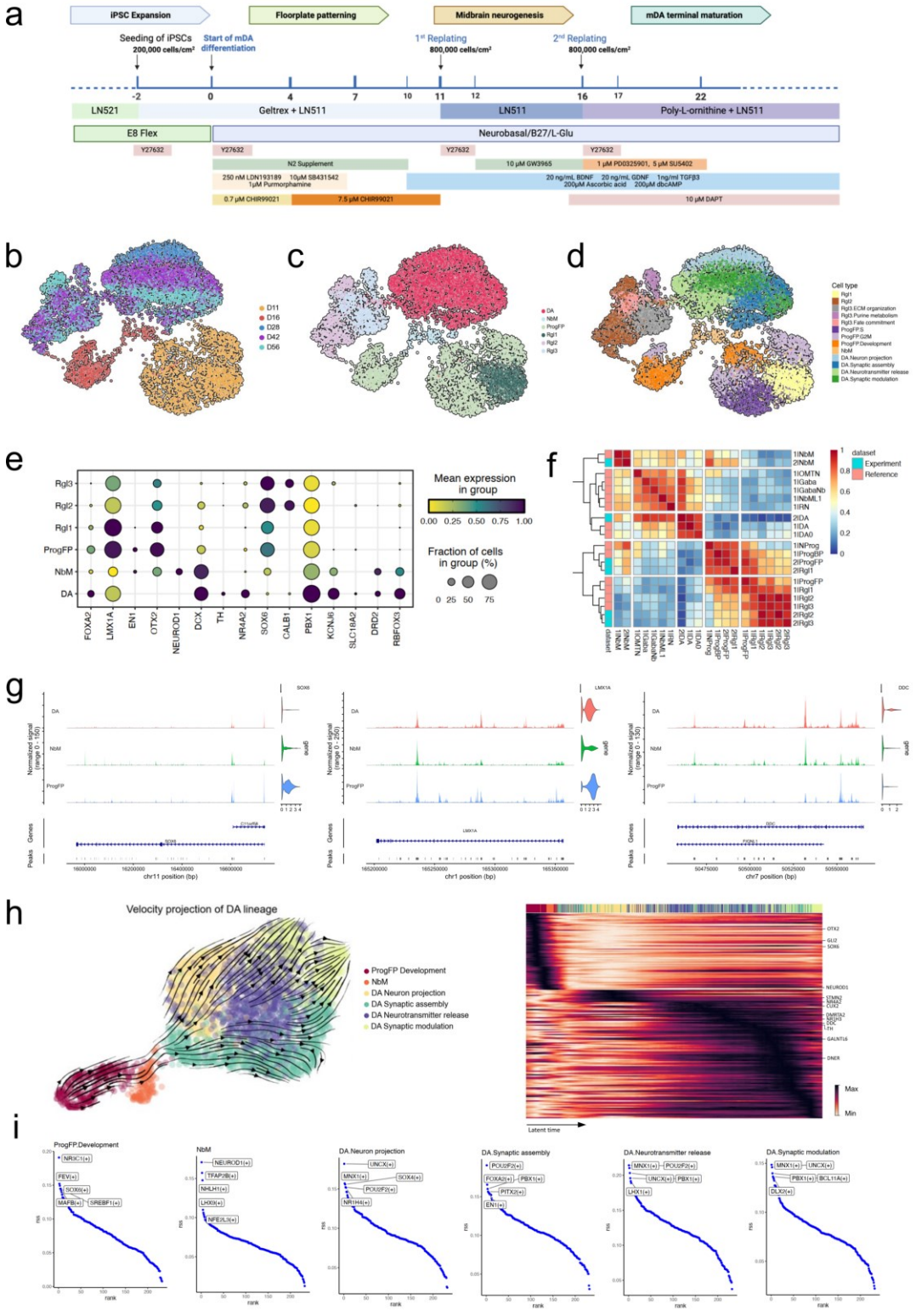

308 **a,** Schematic diagram of the initial differentiation protocol used on the iPSC. **b,** UMAP of time-course
309 samples profiled with simultaneous snRNA-seq and snATAC-seq showing clustering of cells based on both
310 transcriptomic and chromatin accessibility profiles. **c,** Annotated bimodal UMAP clusterings based on
311 major cell types. **d,** Subsets of cell types were manually annotated with top-ranked marker genes and their
312 enriched GO terms. **e,** Dot plot visualizing the expression levels and the percentage of cells expressing
313 curated key genes across cell types during mDA neuron differentiation. **f,** Heatmap of Area Under the
314 Receiver Operating Characteristic Curve (AUROC) scores comparing annotated cell types derived from in
315 vitro differentiation in this study with those from a publicly available first-trimester human midbrain dataset.
316 **g,** Normalized chromatin accessibility tracks at genomic loci of genes of interest (SOX6, LMX1A and
317 DDC), along with enriched accession peaks and links. **h,** UMAP clustering showing RNA velocity
318 projection in mDA-related cell types (left), and a heatmap displaying gene expression dynamics of cluster
319 driver genes ordered by their inferred latent time (right). **i,** Regulon specificity score (RSS) plots
320 highlighting the top five cell type-specific transcription factors involved in mDA differentiation.
321

Fig. 2: Prolonged ventralization promotes accelerated differentiation of mDA neurons.

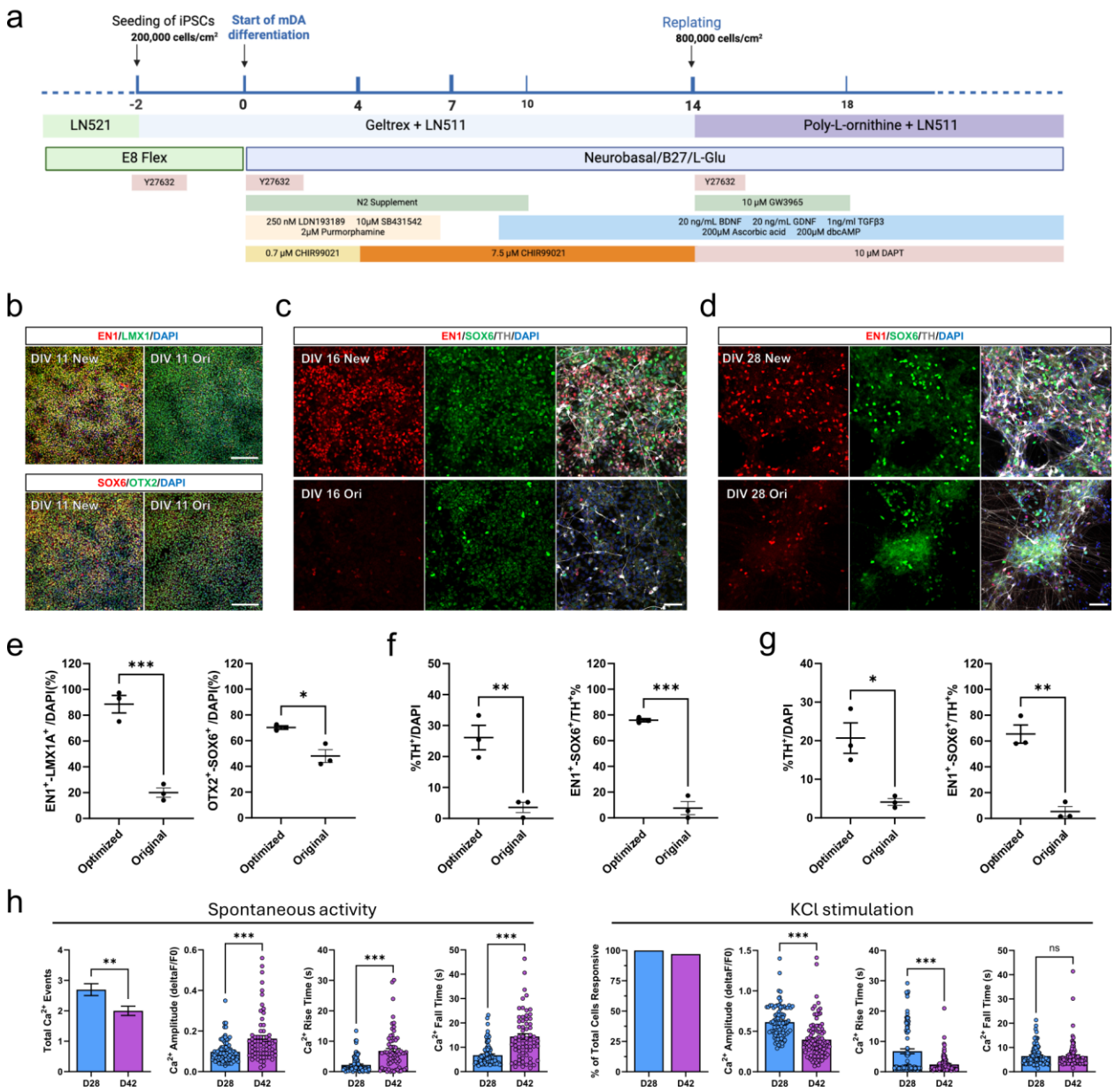

a, Schematic of the optimized differentiation protocol, illustrating the application of pharmacological compounds and growth factors. Representative immunocytochemistry images and quantification from both original protocol and new protocol showing **b,e**, efficacies of midbrain floorplate patterning at DIV11, showing co-localizations of $LMX1^+/EN1^+$ and $SOX6^+/OTX2^+$; and $EN1^+/SOX6^+/TH^+$ neurons at **c,f,** DIV 16 and **d,g,** 28 . White scale bars = 1 mm in B, 50 μm in **c**,**d** (n = 3 biological replicates). **h**, Calcium

330 imaging recordings of spontaneous and KCl-induced activities on DIV 28 and 42, presenting the total
331 number of calcium events per neuron recorded, and the percentages of cells responding to KCl-induced
332 depolarization. Metrics of activities, including amplitude, rise time, and fall time of calcium signals, are
333 depicted in the subsequent bar plots. Each dot represents one cell. Two-tailed T-tests in **e-h** were performed.
334 * = $p<0.05$; ** = $p<0.01$; *** = $p<0.001$. Error bars = SEM.
335

Fig. 3: snRNA-seq confirms enhanced molecular patterning under the optimized protocol.

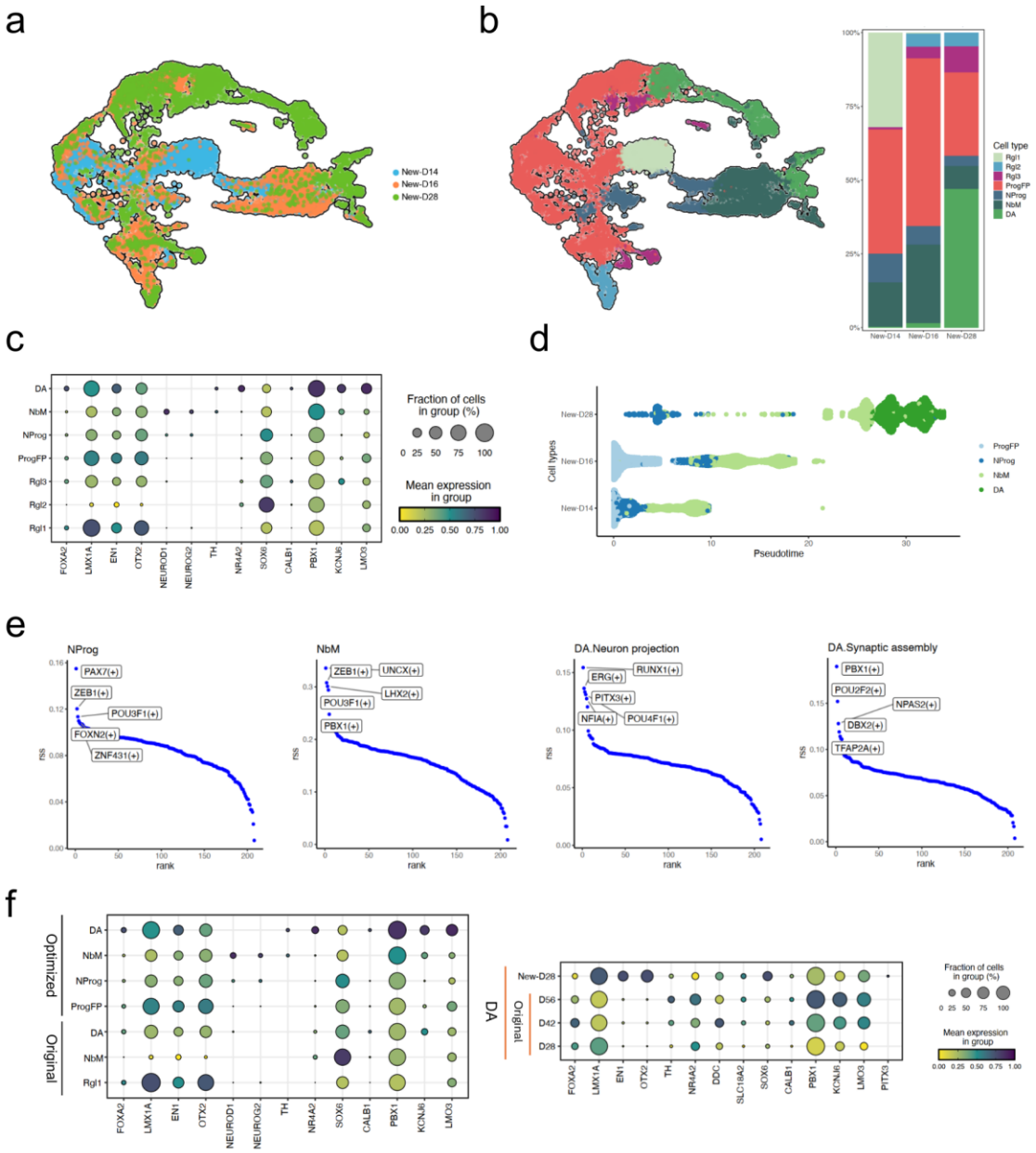

a, UMAP embeddings of mDA differentiation in vitro using KOLF2.1J iPSCs under the new protocol, color coded by different time points at DIV 14, 16 and 28. **b,** UMAP embeddings of detailed cell types were manually annotated using top-ranked marker genes and their enriched GO terms, and proportion of cells classified into each cell type per differentiation time point. **c,** Dot plot visualizing the expression levels and the percentage of cells expressing curated key genes across distinct cell types generated under the new protocol. **d**, Pseudotime trajectory analysis showing progression from progenitor-like populations (ProgFP,

344 NProg, and NbM) to differentiated DA neurons. Cells are ordered by inferred pseudotime along the x-axis.
345 **e**, Regulon specificity score (RSS) plots highlighting the top 5 cell type-specific transcription factors driving
346 mDA differentiation under the new protocol. (f) Dot plots showing the expression levels and the percentage
347 of cells expressing midbrain dopaminergic lineage marker genes after integration in (left) midbrain cells
348 categorized as dopaminergic neurons (DA) (right), dopaminergic lineage cell types across all timepoints
349 and both conditions.
350

Fig. 4: Transplanted neurons restore motor function and mature into A9-subtype mDA neurons *in vivo*.

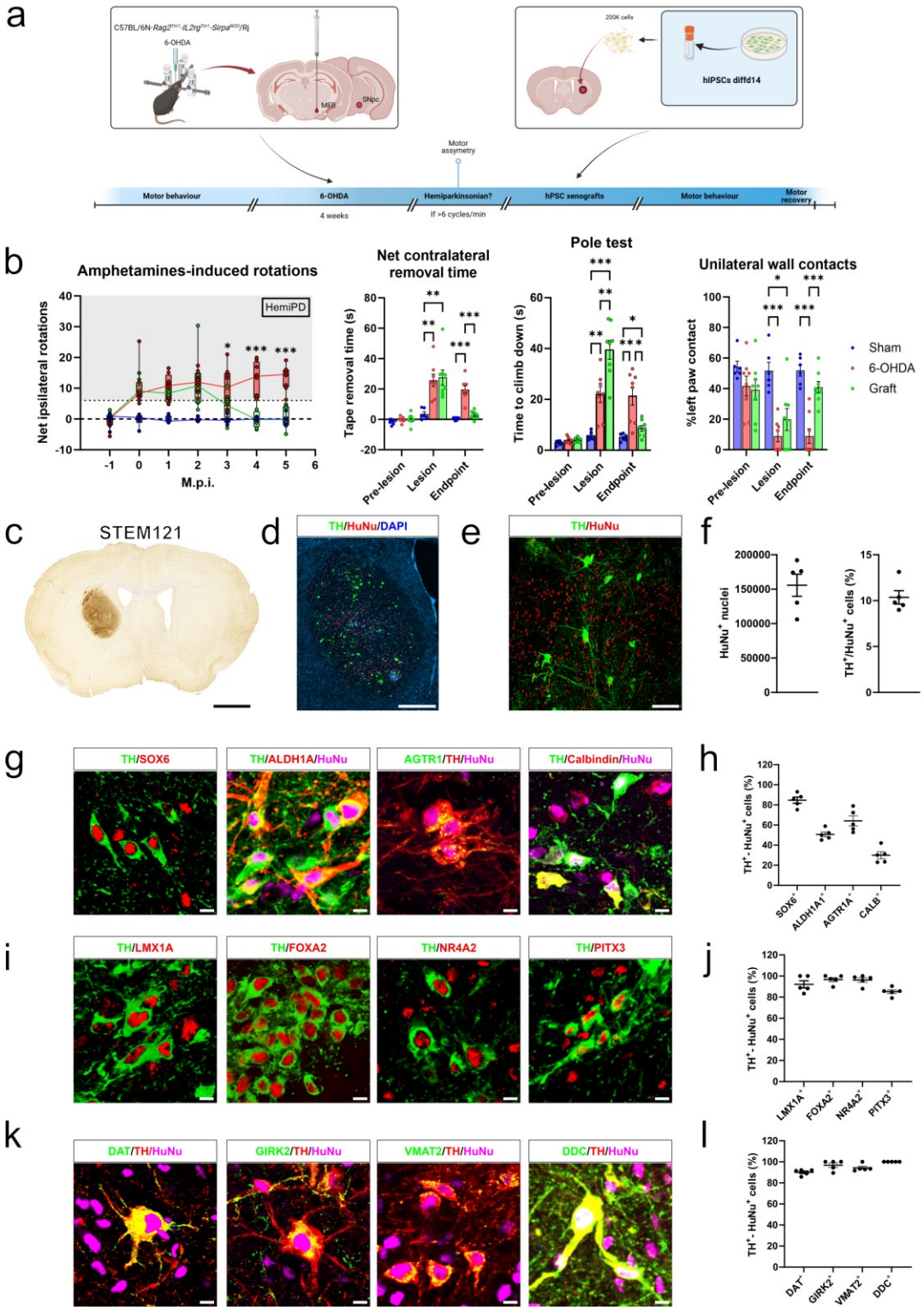

354 **a**, Diagram of the experimental design for the implantation of day 14-differentiated hiPSC in B6RGS mice.
355 **b**, Motor recovery is observed by continuous analysis of amphetamine-induced ipsilateral rotation, endpoint
356 tape removal test, endpoint pole test and endpoint cylinder wall analysis (right). Of note, grafted animals
357 recover pre-lesion state while the 6-OHDA control animals maintain the lesioned state. **c**, Example of
358 grafted tissue, stained against for STEM121, showing the human cells within the graft. **d,** Micrograph of
359 graft stained against for TH and HuNu, showing hDANs all over the graft. **e,** Closeup of grafted hDANs
360 showing elongated and ramified extensions. **f,** Stereological estimate of HuNu+ nuclei (left) and percentage
361 of hDANs (TH+-HuNu+) in grafts (right). **g,** Representative examples of hDANs stained positive for A9-
362 subtype marker, SOX6, ALDH1A1, AGTR1A and A10 marker, Calbindin. **h,** Quantification of percentage
363 of hDANs (TH+-HuNu+) expressing SOX6, ALDH1A1, AGTR1A and Calbindin. **i,** Representative
364 examples of hDANs stained positive for mDA neuron makers, LMX1A, FOXA2, NR4A2 and PITX3. **j,**
365 Quantification of percentage of hDANs (TH+-HuNu+) expressing LMX1A, FOXA2, NR4A2 and PITX3.
366 **k,** Representative examples of hDANs stained positive for proteins involved in DA excretion, DAT, GIRK2,
367 VMAT2 and DDC. **l,** Quantification of percentage of hDANs (TH+-HuNu+) expressing DAT, GIRK2,
368 VMAT2 and DDC. m.p.i = months post-implant. n for animal behavioral experiment **b** = sham: 6; 6-OHDA:
369 8; hIPSC-grafted: 8. N for IHC **f,h,j,l**, = 5. Scale bar = **c**: 1mm; d: 500 µm; **e**: 100 µm; **g,i,k**: 10 µm. Means
370 are represented as bars (**b**) or lines (**f,h,j,l**). One-way ANOVA with Tukey correction between treatments
371 was performed separately on each timepoint in the continuous amphetamine test ($F_{12,114} = 7.876$), as well
372 as for each separate timepoint in the endpoint experiments (Pole test $F_{4,38,} = 27.32$; Tape Removal $F_{4.38} =$
373 8.40; Cylinder Wall $F_{4,38} = 3.97$). * = $p<0.05$; ** = $p<0.01$; *** = $p<0.001$. Error bars = SEM.
374

Fig. 5: snRNA-seq of grafts reveals presence of transcriptionally-defined A9-subtype neurons

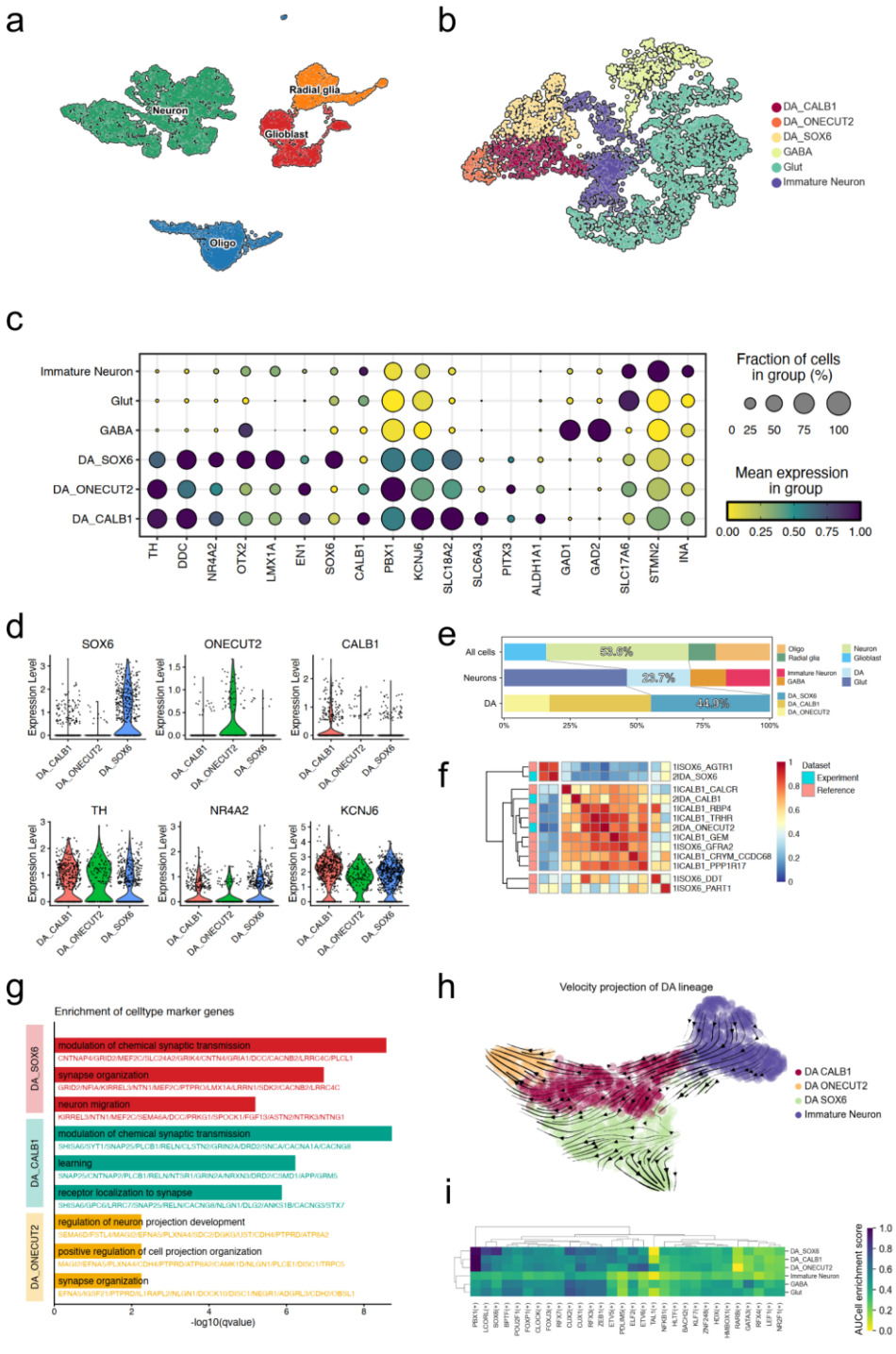

a, Annotated UMAP embeddings of 9,196 high-quality human nuclei recovered from three grafted mice at five months post-transplantation, with cells classified into neurons, radial glia, gliobasts and

380 oligodendrocyte precursors; and **b**, neuronal population was consisted of immature neurons, GABAergic
381 neurons, Glutamatergic neurons and 3 subtypes of mDA neurons, each characterized by specific
382 transcription factors, as DA_CALB1, DA_ONECUT2, and DA_SOX6. **c,** Dot plot showing average gene
383 expression and percentage of expressing cells for selected marker genes across annotated neuronal cell
384 types. **d**, Violin plots of representative marker genes for dopaminergic subtypes (SOX6, ONECUT2,
385 CALB1), pan-DA markers (TH, NR4A2, KCNJ6), illustrating subtype-specific and shared expression
386 patterns. **e**, Average proportion of yielded human nuclei in each cellular hierarchy across three individual
387 datasets, demonstrating consistent representation of DA subtypes (N=3). **f**, MetaNeighbor analysis between
388 transplanted mDA neurons in this study and a reference dataset of DA neurons from the SNpc region of PD
389 patients and matched controls, suggesting transcriptional similarities between DA_SOX6 subtype and
390 SOX6_AGTR1 subtype from the reference dataset. **g,** GO enrichment analysis of DA subtype-specific
391 markers, showing distinct biological processes enriched in DA_SOX6, DA_CALB1, and DA_ONECUT2
392 populations. **h**, RNA velocity projection of mDA neuron trajectories in UMAP embeddings, suggesting
393 differentiation pathways among different DA subtypes and immature neurons. **i**, Heatmap of average
394 regulon activities of the top 30 transcription factors across mDA and other neuronal subtypes.
395

396 ## Discussion

397 This study establishes a multiomic-guided framework for differentiating human iPSCs into mDA
398 neurons with unprecedented molecular and functional fidelity to the PD-vulnerable
399 $SOX6^{+}AGTR1^{+}$ subtype of the substantia nigra. By leveraging single-cell transcriptomic and
400 epigenomic data to identify and overcome a key bottleneck (insufficient ventral patterning), we
401 developed an optimized protocol that achieves accelerated, reproducible production of these
402 therapeutically critical neurons across multiple cell lines.

403 Our longitudinal multi-omic atlas of *in vitro* mDA differentiation revealed stage-specific
404 chromatin accessibility and transcriptional shifts mirroring human midbrain development. Late
405 maturation (DIV42-56) coincided with elevated TH, DDC and KCNJ6 expression, and PBX1
406 regulon activity, a known regulator of mDA survival and functional maturation. Crucially,
407 transcriptome-informed ventralization enhancement (via strategic agonism of SHH signaling)
408 boosted EN1 expression, a key regulator of midbrain identity and a known predictor of transplant
409 success, yielding ventral SNpc neurons with enhanced molecular fidelity to human native
410 counterparts. Furthermore, we were able to identify regulatory networks involving mDA neuron
411 maturation enriched in the new protocol, such as TCF12 and TCF4. Specifically, TCF12 plays a
412 dual role in the early commitment of neural progenitors and the late specification of neuronal
413 subsets, with its loss leading to altered expression of TH and AHD2 (ALDH1A1), the latter being
414 crucial for the specification and maintenance of dopaminergic neurons, particularly in the A9
415 dopaminergic neuronal group[43]. TCF4, on the other hand, is likely involved in the fine-tuning of
416 neuron identity during the onset of mDA neuron subtype specification. In a mouse study, deletion
417 of TCF4 led to delayed maturation of dopaminergic neurons, primarily through transient
418 suppression of *Ahd2* and *Nxph3*[44]. A key advancement in the optimized protocol was the precise
419 modulation of midbrain floor plate (mFP) patterning by the biphasic WNT activation (CHIR boost)
420 and SSH agonism, combined with optimized coating conditions using LN511, which generated a
421 substantial population of mFP progenitors by day 11 and enhanced the expression of critical mDA
422 markers such as FOXA2, LMX1A, and OTX2. This improved patterning was accompanied by a
423 reduced contamination by non-neural cells (a common issue in region-specific neuron generation).
424 Furthermore, the specification to committed progenitors allowed us to omit the MEK/ERK
425 inhibitor PD0325901 and the FGF receptor inhibitor SU5402, previously used to suppress

426 expansion of SOX2^{+} progenitors[45], therefore harnessing the intrinsic neuronal differentiation
427 mechanisms without any further external influence for producing mature mDA neurons
428 downstream. The addition of synthetic LXR ligands (GW3965) further accelerated neurogenesis,
429 leading to the earlier appearance of TH^{+} neurons at day 16 compared to day 21 in prior protocols.
430 This earlier establishment enables functional assays (such as calcium imaging and neurotransmitter
431 release analysis) to be performed sooner, thereby expediting detection of phenotypic differences.
432 As an example, live-cell calcium recordings confirmed that the derived mDA neurons displayed
433 spontaneous electrical activity and robust depolarization responses, consistent with functionally
434 active neurons[46]. This protocol also proved reproducible across multiple iPSC lines, including
435 those from Parkinsonian patients, highlighting its potential as a standardized approach for
436 generating patient-targeted high-quality dopaminergic neurons, a crucial step for modeling
437 neurodegenerative diseases and testing therapeutic strategies. Finally, as a proof-of concept
438 validation for therapeutic approaches, we determined that the new protocol could produce mFP
439 progenitors and NbM able to differentiate *in vivo* to mDA neurons resembling the A9-subtype
440 nigral neurons in majority, based on expression of proteins such as SOX6, AGTR1, GIRK2 or
441 ALDH1A, reported to be more susceptible to PD in human and animal models[19,40,47,48].
442 Furthermore, evaluation of the transcriptomic profile of the DA neurons in the graft showed high
443 resemblance to the human counterpart, specially the SOX6-AGTR1A mDA neurons. Moreover,
444 the lack of proliferative progenitor cells at our endpoint is promising for putative long-term
445 transplants. This proposes that these cells could have great potential for directed replacement
446 therapies. While these advancements could be of great interest to the PD research community, we
447 have to address several caveats. First, we only have established the replicability of this protocol
448 on hIPSC, both WT and with GBA mutations. But further in-depth characterization with more well

449 known mutations found in familial PD, such as GBA^{E326K}, LRRK2^{G2019S} or the triplicate SNCA,
450 could elucidate the validity of this enhanced protocol. Furthermore, the use of human embryonic
451 stem cells has not been proposed for this study. More *in vitro* studies would be of interest to
452 validate further this new protocol. Another caveat to address is the pre-clinical aspect, as the *in*
453 *vivo* experiments were only used as proof-of-concept for therapeutical approaches. Further grafting
454 experiments with PD-mutated hiPSC cell lines and a more in-depth preclinical analysis could detail
455 if this protocol would be a much better advantage that the current available protocols, which so far
456 have shown to be safe in clinical trials[12,13]. Moreover, the longevity of the grafting experiment was
457 decided upon stable motor recovery, so we do not have an overview of the long-term effects of
458 these grafts, whether other contaminants can appear or tumorigenesis in aged individuals. In
459 conclusion, we have developed a multiomic-guided differentiation protocol which addresses the
460 major challenge of subtype specificity in generating human mDA neurons relevant to PD. By
461 leveraging single-cell genomics and epigenomics to identify and correct insufficient ventral
462 patterning, we achieved robust enrichment of the PD-vulnerable SOX6^{+} A9 subtype, which yielded
463 neurons with enhanced molecular fidelity, functional maturity, and the capacity to restore motor
464 function upon transplantation. Our work provides a robust platform for generating more accurate
465 human cellular models of PD and establishes a foundational strategy for developing next-
466 generation, subtype-enriched cell replacement therapies.
467

468 **Methods**

469 Cell lines

470 KOLF 2.1J cell line was obtained through Jackson Laboratories[49]. GBA1^{E326K} heterozygous PD
471 patient-derived iPSCs (NH50143) along with its edited isogenic control iPSCs (NH50142) were
472 obtained from the Rutgers University Cell and DNA Repository (RUCDR). All experiments
473 performed with these cells followed the Ethical Permit 2021-06727-01 issued by the Swedish
474 Ethical Review Authority. Karyotipe by G-banding, genotypes by polymerase chain reaction
475 (PCR), pluripotency by pluripotency marker microscopy analysis, and mycoplasma infection by
476 PCR were routinely assessed before starting new experiments. Applied iPSC lines were adapted
477 to grow on Laminin 521 (Biolamina, LN521)-coated plates and maintained in Essential 8 Flex
478 media (E8 Flex, Thermo Fisher Scientific) at 37ºC, 5% CO2, until starting differentiation. The
479 medium was changed daily, and cells were passaged at 70% confluency using TrypLE™ Select
480 Enzyme (Thermo Fisher Scientific) at a 1:20 ratio. When thawing and replating, 10 μM Rho-
481 associated protein kinase (ROCK) inhibitor (Y-27632) (Tocris) was added into the culture media
482 overnight.

483 ## Midbrain dopaminergic neuron differentiation

484 Two days prior to the mDA differentiation, adapted iPSC cells were seeded at a density of 200,000
485 cells/cm2 onto plates coated with Geltrex (Life Technologies) and Laminin-511 (Biolamina,
486 LN511), and maintained in E8 Flex media (Thermo Fisher Scientific) for expansion. The
487 differentiation protocol was initiated when the cells reach approximately 80% confluency. For the
488 first iteration, cells were cultured at day 0-4 on plates coated with Geltrex and LN511, replated at
489 day 11 on LN511, and replated again at day 16 on LN511 + poly-L-ornithine. Cultured cells were
490 kept in Neurobasal/N2/B27 (Life Technologies) medium and 2 mM L-glutamine (Invitrogen),
491 along with various supplements for the first stage of the protocol. From day 0 to day 4, the culture
492 medium was conditioned with 250 nM LDN193189 (Stemgent), 10 μM SB431542, 1 μM

493 Purmorphamine, and 0.7 μM CHIR99021 from day 0 to day 3, with the inclusion of 10 μM Y27632
494 (Tocris Bioscience) during the first 24 hours. Boosted CHIR99021 (7.5μM) was administered from
495 day 4 to day 11, while LDN193189, SB431542 and Purmorphamine were withdrawn after day 7
496 and N2 supplement after day 10. From day 10 to day 28, cells were switched to the differentiation
497 media: Neurobasal/B27/L-Glu media supplemented with 20 ng/mL brain-derived neurotrophic
498 factor (BDNF, R&D Systems), 20 ng/ml glial cell line-derived 455 neurotrophic factor (GDNF,
499 R&D Systems), 1 ng/ml transforming growth factor type b3 (TGFb3, R&D Systems), 0.2 mM
500 ascorbic acid (Sigma), 0.2 mM Dibutyryl cAMP (Sigma). On day 11 and 16, the resulting cells
501 were dissociated into single cells, replated at a density of 800,000 cells/cm2 onto plates coated
502 with LN511 and polyornithine/LN511 respectively, and treated with 10 μM Y27632 for 48 hours.
503 To promote neurogenesis, the mDA differentiation media was supplemented with 10 μM DAPT
504 (Sigma) from day 16. The small molecule GW3965 (10 μM) was administered from day 12 to day
505 15, followed by a cocktail of small molecules consisting of 1 μM PD0325901 and 5 μM SU5402
506 (Sigma), from day 16 to day 21. For the second iteration, conditions were similar except for the
507 following: Culture plates were coated with Geltrex + LN511 until day 14, and poly-L-ornithine +
508 LN511 from day 14 onwards. Cells were only replated once at day 14 and boosted CHIR99021
509 (7.5μM) was administered from day 4 to day 14. Day 0-7 Purmorphamine concentration was
510 increased to 2 μM, and both PD0325901 and SU5402 were removed from the protocol.

511 Immunocytochemistry

512 Progenitor cells at different stages were seeded in a 96-well plate at a density of about 300,000
513 cells per well for the intended cell culture purposes. Harvested cells were fixed by 4%
514 paraformaldehyde (PFA) for 20 min at 4ºC, and then pre-incubated by 5% donkey serum in
515 phosphate buffered saline containing 0.3% Triton X-100 (PBST) for 1 hour. The samples were

516 incubated with primary antibodies at 4ºC overnight. The samples were incubated with either
517 Alexa488 or Alexa555 or Alexa647-conjugated secondary antibodies (Thermo Fisher Scientific)
518 for 30 min and then were incubated with 4',6-diamidino-2-phenylindole (DAPI, Sigma, D9542)
519 for 15 min. The primary antibodies were used as follows: CORIN (rat, 1:1,000, R&D Systems,
520 MAB2209), DCX (goat, 1:500, SantaCruz, sc-8066), EN1 (mouse 1:50, DSHB, 4G11), FOXA2
521 (goat, 1:500, R&D Systems, AF2400), GIRK2 (rabbit, 1:400, Alomone, APC006), LMX1A
522 (rabbit, 1:4,000, Millipore, AB10533), LMO3 (goat, 1:200, SantaCruz, sc-82647), MAP2 (mouse
523 1:1,000, Sigma, M4403), NURR1 (rabbit, 1:500, SantaCruz, sc-990), OTX2 (goat, 1:1,000, R&D
524 Systems, AF1979), TH (rabbit, 1:1,000, Millipore, AB152), TH (mouse, 1:500, ImmunoStar,
525 22941), and TH (sheep, 1:500, Novus Biological, NB300). Mounted cells were further visualized
526 using confocal microscopy (Zeiss LSM880 or 980) with a 10X or 20X lens. Quantification of
527 images was performed using QuPath[58] by generating a "single measurement classifier" or
528 "composite classifier" for positive or double-positive cells respectively.

529 ## Calcium imaging

530 The 35mm culture dishes were loaded with the $Ca2^{+}$-sensitive fluorescence indicator Fluo-4/AM
531 (5 µM; Invitrogen, USA) and Pluronic F-127 (0.625%, ThermoFisher Scientific) and incubated
532 for 30 min at 37ºC in Krebs-Ringer buffer, containing: NaCl (119 mM), KCl (2.5 mM), NaH2PO4
533 (1 mM), CaCl2 (2.5 mM), MgCl2 (1.3 mM), HEPES (20 mM) and D-Glucose (11 mM), with pH
534 adjusted to 7.4. Dishes were washed twice and $Ca2^{+}$-measurements were performed in Krebs-
535 Ringer buffer at 37ºC on a confocal spinning disk microscope (Nikon CrEST X-Light V3)
536 equipped with a 20x Air lens. Excitation was assessed at 480 nm at a sampling frequency of 1 Hz.
537 The equipment was controlled, and data was acquired using the Nikon NIS-Elements software.

538 FIJI, MATLAB (R2020b, MathWorks, USA) and FluoroSNNAP (https://github.com/tapan-
539 patel/FluoroSNNAP) were used to process and analyze the data.

540 Single cell sequencing libraries preparation and data processing

541 A total of 5 samples (DIV 11, 16, 28, 42, and 56) from KOLF2.1J mDA neuron cultures generated
542 with the optimized protocol were collected for time-course multiomic analysis (ATAC + Gene
543 Expression); in addition, 3 samples (DIV 14, 16, and 28) from the new protocol trial of KOLF2.1J
544 mDA differentiation were collected for single-nuclei transcriptomic profiling. All 8 samples were
545 prepared with commercially available protocols (10x Genomics) and the resulting Fastqc files
546 were processed through the 10X Genomics Cellranger pipeline[50], while 5 multiomic libraries were
547 aligned to the hg38 reference genome using Cellranger-arc default settings[51]. After quality-control
548 filtering, we obtained high-quality 23,534 cells (Fig. 3a, Extended Fig. 5a) and then we integrated
549 transcriptomic profiles from both conditions using Harmony[52], enabling a comparative analysis by
550 isolating the mDA neuronal lineage from different datasets (Extended Fig. 5b). Resulting
551 transcriptomic and epigenomic data from individual samples were combined by projects using the
552 'aggr' function in Cellranger or Cellranger-arc, without normalization applied. Objects produced
553 with Seurat V4.4.0 were employed to accommodate aggregated count matrix[53], with the fragment
554 files specifically integrated into Signac v1.9.0 chromatin assays[54]. Quality metrics for gene
555 expression and peak accessibility, such as mitochondrial ratio, cell cycle score, nucleosome signal,
556 and Transcription Start Site (TSS) enrichment, were thereafter calculated to determine quality
557 control cutoffs. Depending on sample quality, following thresholds were applied for downstream
558 analysis: a maximum of 300,000 and a minimum of 1,000 ATAC counts per cell, a maximum of
559 25,000 and a minimum of 600 RNA counts, at least 250 genes detected, a maximum nucleosomal
560 signal of 1.5, TSS enrichment of at least 2, and mitochondrial content no higher than 15%. These

561 cutoffs reduced the cell count by less than 20% without significantly affecting clustering
562 downstream. Peak calling was performed with MACS2 v2.2.9 using the aggregated fragments
563 file[55], and those mapped to non-standard chromosomes or overlapping hg38 genome blacklist
564 regions were excluded. DoubletFinder v2.0 was applied to identify doublets in gene expression
565 data by flagging instances with a high resemblance to artificial neighbors in gene expression
566 space[56]. AMULET (ATAC-seq MULtiplet Estimation Tool) was additionally utilized to detect
567 potential multiplets in snATAC-seq datasets by enumerating regions with greater than two
568 uniquely aligned reads across the genome[57]. All predicted doublets were removed from the
569 downstream analysis. After merging high-quality cells from the relevant projects, count data was
570 normalized using SCTransform V2 function with regression out of mitochondrial or cell-cycle
571 genes. The top 2,000 most variable genes were initially identified through variance-stabilizing
572 transformation, along with 95% of the most frequent peaks in multiomic datasets, as a part of the
573 significant feature selection process. Subsequent dimensionality reduction was performed using
574 the principal components analysis (PCA), in which the top 30/40 principal components were
575 chosen from the elbow plot to represent most of the diversity of datasets. For single-nuclei ATAC-
576 seq datasets, singular value decomposition (SVD) was performed with the top 25 of the Latent
577 Semantic Indexing (LSI) layers to reduce the dimensions of the most common peaks. Notably, the
578 first LSI component was excluded from downstream analysis as it often captures sequencing depth
579 (technical variation) rather than biological variation. Putative clusters were identified by a spiking
580 neural network (SNN) modularity optimization-based clustering algorithm, and the optimal
581 resolution of clustering was determined by iterating over different resolution for the most stable
582 segregation. Finally, the calculated nearest-neighbor graph was projected to two dimensions to
583 visualize the distribution of instances by representing with uniform manifold approximation and

584 projection (UMAP). To accurately identify and interpret cell states *in vitro*, we leveraged
585 combined manual cell type annotation using cluster-specific marker genes[58,59], with automatic
586 annotation methods using reference datasets that characterize first-trimester developing human
587 brain[14,60]. Initially, a label transfer was performed with Celltypist[61] and 'TransferData' function in
588 Seurat to automatically classify selected dataset with cell type labels from the reference dataset,
589 based on the similarity of query gene expression profiles to selected anchors in the reference
590 dataset. The identity of each cell will be determined by the highest prediction score, and for
591 stringent comparison, cells with a prediction score below 0.51 will be excluded from downstream
592 analysis. After data trimming and reclustering, a manual cluster-based annotation was performed,
593 using both expression levels of canonical midbrain development marker genes and top 50
594 upregulated genes identified by the 'FindAllMarkers' function. These upregulated genes were used
595 for pathway and biological process enrichment analysis via Metascape[59], and the top-ranked terms
596 were used to refine annotations and determine cell subtypes or states. To reconstruct the putative
597 trajectory of mDA differentiation *in vitro*, we employed Monocle3[62] and scVelo[63,64] to infer
598 pseudo- and latent-temporal ordering of cells using default parameters[65]. The root of trajectory for
599 pseudotime analysis was set as ProgFP or NbM at the earliest timepoint. at the earliest timepoint.
600 To represent quantitatively the cell identity similarities with other published human datasets, we
601 performed Metaneighbor[66]. SCENIC[67] was used to visualize regulatory networks and regulon in
602 our developing cells using AUCell scores.

603 Animals

604 Healthy female adult (8-12 weeks old) C57BL/6N-Rag2Tm1-IL2rgTm1-SirpaNOD/Rj (B6RGS)
605 mice were purchased from Janvier Labs. Groups of 5 animals were housed in ventilated cages
606 under a 12 h light-dark cycle with food (standard chow) and water ad libitum at 20-22ºC and 50-

607 55% humidity. Tunnels, cardboard nesting material and chewing wooden bars were used for
608 environmental enrichment. All surgical procedures followed aseptic techniques, and for post-
609 surgical recovery, additional Dietgel Recovery (Scanbur) and food pellets were supplied on the
610 cage floor. Animals were randomly allocated to sham control group (n=6), hemiPD group (n=8)
611 and a grafted group (n=8), ensuring all cages had individuals of each group. Briefly, the exclusion
612 criteria were animals which lost over 10% of their pre-surgical weight after 4 weeks were discarded
613 from the experiment. No animals were discarded based on this criterion. The experimental unit
614 were the individual mouse. All procedures were approved by the local ethical committee
615 (Stockholms djurforsoksetiska namnd) and followed the EU directive 2010/63/EU under the
616 ethical permit of Ernesto Arenas Cases and Sandra Gellhaar (12265-2021; 2-3143/23; 2-3595/24;
617 2-3147/24).

618 ## 6-OHDA mouse model

619 B6RGS mice were acclimatized 2-3 weeks before surgery to the animal facility and the researcher
620 and to a recovery diet 2-3 days before surgery. For 6-hydroxidopamine (6-OHDA, Sigma) lesions
621 (or sham), animals were injected analgesia (Carprofen 5mg/kg + Buprenorphine 0.1 mg/kg) 15
622 minutes before isoflurane induction (4%). Animals were anesthetized at 1-2% isoflurane in air and
623 injected intracranially (ICR) using a Neurostar Robotic Stereotaxic Frame equipped with a 10 µl
624 syringe with 33G blunt needle (Hamilton) 1 µl of 6-OHDA 3.6 µg/ µl in sterile ascorbic acid/saline
625 0.02% (or sham vehicle) in the right medial forebrain bundle [respect to Bregma: AP -1.2 mm,
626 ML +1.2 mm, DV -5.0 mm] at a flow of 0.2 µl/min, raising the needle 500 µm for 3 minutes. The
627 needle was left inside for 2 additional minutes. Animals were placed in warm cages (28 °C)
628 between 3 days and 1 week for better recovery and rehydrated with Ringer Acetate solution if
629 weight decreased by 5%. 6-OHDA hemiPD was confirmed by amphetamine-induced rotation.

630 Briefly, 4 weeks after the lesion, mice were injected intraperitoneally with d-amphetamine in saline
631 (5 mg/kg). 10 minutes after injection, the mice were recorded for 30 minutes inside a 15 cm wide
632 cylinder in dark conditions, and the number of net ipsilateral rotations (ipsilateral-contralateral)
633 per minute in active movement was calculated using Ethovision XT 17 (Noldus). Mice are
634 considered hemiPD if the values are >6 rotations/minutes.

635 hiPSC transplant

636 HemiPD-confirmed mice of healthy weight (22-30 g) were randomly selected for ICR hPSC
637 injection in the right striatum [respect to Bregma: AP +0.5 mm, ML +2 mm, DV -3.5 mm].
638 Analgesia and anesthesia were followed as above. For ICR transplants, 2 µl of 100.000 ± 20.000
639 hPSCs/µl in Neurobasal medium was injected to achieve 200.000 hPSC transplants. For cell
640 injection, the Neurostar robot was coupled with a 10 µl syringe with a 27G sharp syringe. A flow
641 of 0.5 µl/min was used, and the needle remained for 5 additional minutes. Cells were injected
642 between 1-6 hours after thawing.

643 Amphetamines-induced rotations

644 Mice were analysed a week before surgery, 4 weeks after surgery and hereon once a month until
645 endpoint was reached. Mice were injected intraperitoneally with 5 mg/kg d-amphetamine in saline
646 (0.5 mg/ml). 10 minutes after injection, the mice were recorded for 30 minutes inside a 15 cm wide
647 cylinder in dark conditions, and the number of net ipsilateral rotations (ipsilateral-contralateral)
648 per minute in active movement (body center traveling at >0.5 cm/s) was calculated using
649 Ethovision XT 17.

650 Pole test

651 Mice were analysed a week before surgery, 4 weeks after surgery and at the endpoint. Animals
652 were placed facing upwards on the top of a 20 cm vertical smooth wooden pole with 2 mm grooves
653 notched every 0.5 cm down. The time to climb down was counted starting when the mouse rotates
654 facing downwards. Animals were trained for a minimum of 2 days before testing day, by
655 performing 3 mock tests each day. If the animals took more than 1 minute to descend, the trial was
656 interrupted and repeated at least 10 minutes later. A total of 3 trials were used to calculate a mean
657 value per animal.

658 Cylinder wall

659 Mice were analysed a week before surgery, 4 weeks after surgery and at the endpoint. Animals
660 were placed inside a 12 cm diameter glass cylinder in red light and quiet conditions. For 15
661 minutes, animals were recorded and videos were analysed at x8 speed. Unilateral full paw contacts
662 were counted. Paw dragging or paws not fully placed on glass were disregarded.

663 Tape removal test

664 Mice were analysed a week before surgery, 4 weeks after surgery and at the endpoint. A green
665 adhesive paper tape 2x3 mm was placed on each paw individually. The time it took to remove the
666 tape was counted, beginning when the mouse recognized it and ending when it was removed from
667 the paw. Net contralateral time (ipsilateral-contralateral) was calculated to better visualize and
668 eliminate external factors. Before testing day, animals were trained for a minimum of 2 days,
669 performing 3 mock trials for each paw. If the animal took more than a minute, the trial was
670 interrupted and repeated at least 15 minutes later. A total of 3 trials were used to calculate a mean
671 value.

672 Immunohistochemistry

673 5 animals were terminally anesthethized with IP pentobarbital 100 mg/kg dose and then perfused
674 intracardially with 50 ml of pH-corrected PBS1X followed by 50 ml of formaldehyde 4 % (FA)
675 both at a flow of 9 ml/min. Brains were extracted and placed in FA overnight, after which they
676 were placed in sucrose 30%/PBS solution at 4ºC for 2-3 days. After, brains were kept at -80ºC.

677 Brains were equilibrated at -20ºC for 4 hours before slicing. Samples were sliced in series at -20ºC
678 at 20 µm using a Cryostar NX70 (Epredia) and stored for further use at -20ºC in cryoprotective
679 solution (Ethylenglycol 30%, Glycerol 30%, PBS1X). A total of 5 brains were processed.

680 Samples were stained using free-floating protocols. Briefly, 2 series of 5 minutes of PBS1X,
681 followed by 15 minutes of PBS-TritonX 0.3% (PBTx0.3%), then 2 series of 5 minutes of
682 PBTx0.1%. Samples were blocked for 1 hour with blocking solution (BSA 1 mg/ml, Normal
683 Donkey Serum 5%, PBTx0.1%) and incubated o/n at 4ºC with primary antibody diluted in
684 blocking solution. Primary antibody was washed with 2 series of 5 minutes PBTx0.1% and
685 samples were incubated for 4 hours with secondary antibody diluted in blocking solution and
686 washed twice for 5 minutes with PBS1X. Tissue was counterstained with DAPI 1:1000 in PBS1X
687 for 10 minutes and then washed twice for 5 minutes with PBS1X. Stained samples were mounted
688 on Superfrost Plus slides (Epredia) and Fluoromount-G mounting medium (00-4958-02, Thermo
689 Scientific). Primary antibodies used were STEM121 (mouse, 1:1000, Tanaka Bio, Y40410), TH
690 (rabbit, 1:1000, Pelfreeze, P4010; sheep, 1:250 Pelfreeze, P60101), HuNu (mouse, 1:1000,
691 Millipore, MAB1281), SOX6 (rabbit, 1:200, Abcam, ab30455), ALDH1A (rabbit, 1:500, Atlas
692 Antibodies, HPA002123), AGTR1 (rabbit, 1:100, Invitrogen, MA5-56587), Calbindin-1 (rabbit,
693 1:200, Invitrogen, PA5-85669), LMX1 (rabbit, 1:100, Millipore, AB10533), FOXA2 (rabbit,
694 1:200, Cell Signaling, 3143S), NR4A2 (rabbit, 1:500, Invitrogen, PA5-78097), PITX3 (rabbit,
695 1:100, Invitrogen, 35-2850), DAT (rat, 1:250, Abcam, ab5990), GIRK2 (rabbit, 1:500, Alomone

696 Labs, APC006), VMAT2 (rabbit, 1:500, Sigma-Aldrich, AB1598P), DDC (rabbit, 1:500, Novus
697 Biological, NB300-252), Ki67 (rabbit, 1:200, Abcam, ab15580), SOX2 (goat, 1:200, R&D
698 Systems, AF2018). All fluorescent secondary antibodies were from Invitrogen, donkey as host and
699 conjugated with Alexa Fluor 488, 555 or 647. The HRP-conjugated antibody was a goat anti-
700 mouse from Invitrogen. Images were captured either with laser confocal microscope Zeiss
701 LSM800 equipped with x20 lens or high-throughput epifluorescence microscope Zeiss Axioscan
702 equipped with x10 lens. Quantification of images was performed using QuPath[58] by generating a
703 'single measurement classifier' or 'composite classifier' for positive or double-positive cells
704 respectively.

705 Single-nuclei RNA sequencing of grafts and data analysis

706 3 animals were euthanized by cervical dislocation and brains were promptly extracted and flash-
707 frozen in dry-ice chilled isopentane for 10-15 seconds. Flash-frozen brains were stored at -80 °C
708 until graft extraction. A total of 3 brains with grafts were processed independently.

709 On the day of nuclei extraction, brains were equilibrated to -20ºC and sliced in -20ºC cooled
710 chambers. Brain matrices were used to stabilize the brain, and 1 mm-thick slices for a total of 4 (2
711 before the center of graft implant location and 2 after) were cut using chilled razors. 1 mm punches
712 of each slice of the dorsal striatum were extracted using 1 mm biopsy-punchers (49101, PFM
713 Medical).

714 Nuclei were dissociated using the 10X Genomics Chromium nuclei extraction kit (1000494) using
715 manufacturer's instructions. For better extraction, eppendorfs used for tissue dissociation were
716 coated with BSA 1% o/n at 4ºC, briefly washed with filtered sterile PBS1X before procedure. 10X
717 Genomics Chromium GEM-X Single Cell 3' Kit v4 (1000691), Chromium GEM-X Single Cell 3'

718 Chip Kit v4 (1000690) and Dual Index Kit TT Set A (1000215) were used for GEM generation
719 using manufacturer's instructions with the 10X Controller iX. GEMs were sent for RNA-
720 sequencing to National Genomics Infrastructure of SciLifeLab (Karolinska Institute, Sweden)
721 using the NovaSeq XPlus 25B. Data analysis was performed as the *in vitro* RNAseq dataset,
722 described above. To ensure analysis of human cells, we aligned the libraries to the h38 human
723 genome dataset and the m39 mouse genome dataset, and cells with a ratio of human:mouse gene
724 count >1 were processed.

725 Statistics

726 The N for the animals was calculated using G-Power 3.1[68] based on prior data from several
727 publications of hemiPD rodent model behavior[69]. Briefly, using the "ANOVA: repeated measures,
728 between factors" a priori statistical test, the effect size was calculated to be 0.82, α =0.05, β=0.95,
729 groups =3, measurements=7 and correlation among repeated measurements=0.8.

730 GraphPad Prism v10.00 was used for generating all graphs and performing statistical analyses. For
731 pairwise comparisons, Two-tailed Student's t-test was utilized. One-way ANOVA or two-way
732 ANOVA with Tukey's or Bonferroni's multiple comparison tests were used to compare multiple
733 variables. Error bars indicate the standard error of the mean (SEM). F are reported with degrees of
734 freedom for numerator and denominator ($F_{DFn,DFd}$). Significance levels were set as follows: ns =
735 not significant; * = $p<0.05$; ** = $p<0.01$; *** = $p<0.001$; **** = $p<0.0001$.

736 **Data Availability**

737 Single-cell RNA-seq and ATAC-seq raw data have been deposited at EGA (EGA accession
738 number: EGAD50000002054). Key Resource Table (including Material RRID, protocol.io links
739 for protocols used, accession numbers for sequencing datasets), microscopy data and images have

been deposited at Zenodo at https://doi.org/10.5281/zenodo.17099441 and are publicly available as of the date of publication. All reused code used for this paper has been deposited at Github and linked to Zenodo at https://doi.org/10.5281/zenodo.17099441 and is publicly available as of the date of publication. This paper analyzes existing, publicly available data, accessible at https://doi.org/10.1038/s41593-022-01061-1; https://doi.org/10.1126/science.adf1226; https://doi.org/10.1126/science.add7046. Any additional information required to reanalyze the data reported in this paper is available from the lead contact upon request.

Code Availability

No new or original code was generated for this paper.

References

1. Poewe, W. *et al.* Parkinson disease. *Nat Rev Dis Primers* **3**, 17013 (2017).
2. Brichta, L., Greengard, P. & Flajolet, M. Advances in the pharmacological treatment of Parkinson's disease: targeting neurotransmitter systems. *Trends Neurosci* **36**, 543–54 (2013).
3. Björklund, A. & Parmar, M. Dopamine Cell Therapy: From Cell Replacement to Circuitry Repair. *J Parkinsons Dis* **11**, S159 (2021).
4. Doi, D. *et al.* Isolation of human induced pluripotent stem cell-derived dopaminergic progenitors by cell sorting for successful transplantation. *Stem Cell Reports* **2**, 337–350 (2014).
5. Kim, T. W. *et al.* Biphasic Activation of WNT Signaling Facilitates the Derivation of Midbrain Dopamine Neurons from hESCs for Translational Use. *Cell Stem Cell* **28**, 343-355.e5 (2021).
6. Kriks, S. *et al.* Dopamine neurons derived from human ES cells efficiently engraft in animal models of Parkinson's disease. *Nature* **480**, 547–551 (2011).
7. Nishimura, K. *et al.* Single-cell transcriptomics reveals correct developmental dynamics and high-quality midbrain cell types by improved hESC differentiation. *Stem Cell Reports* **18**, 337–353 (2023).

768 8. Kirkeby, A. *et al.* Preclinical quality, safety, and efficacy of a human embryonic stem cell-
769 derived product for the treatment of Parkinson's disease, STEM-PD. *Cell Stem Cell* **30**,
770 1299-1314.e9 (2023).

771 9. Piao, J. *et al.* Preclinical Efficacy and Safety of a Human Embryonic Stem Cell-Derived
772 Midbrain Dopamine Progenitor Product, MSK-DA01. *Cell Stem Cell* **28**, 217-229.e7
773 (2021).

774 10. Schweitzer, J. S. *et al.* Personalized iPSC-Derived Dopamine Progenitor Cells for
775 Parkinson's Disease. *N Engl J Med* **382**, 1926–1932 (2020).

776 11. Takahashi, J. iPS cell-based therapy for Parkinson's disease: A Kyoto trial. *Regen Ther*
777 **13**, 18–22 (2020).

778 12. Tabar, V. *et al.* Phase I trial of hES cell-derived dopaminergic neurons for Parkinson's
779 disease. *Nature 2025 641:8064* **641**, 978–983 (2025).

780 13. Sawamoto, N. *et al.* Phase I/II trial of iPS-cell-derived dopaminergic cells for Parkinson's
781 disease. *Nature 2025 641:8064* **641**, 971–977 (2025).

782 14. Braun, E. *et al.* Comprehensive cell atlas of the first-trimester developing human brain.
783 *Science* **382**, eadf1226 (2023).

784 15. La Manno, G. *et al.* Molecular Diversity of Midbrain Development in Mouse, Human, and
785 Stem Cells. *Cell* **167**, 566-580.e19 (2016).

786 16. Xu, P. *et al.* Human midbrain dopaminergic neuronal differentiation markers predict cell
787 therapy outcomes in a Parkinson's disease model. *J Clin Invest* **132**, (2022).

788 17. Tiklová, K. *et al.* Single-cell RNA sequencing reveals midbrain dopamine neuron
789 diversity emerging during mouse brain development. *Nature Communications 2019 10:1*
790 **10**, 1–12 (2019).

791 18. Greene, P. E. *et al.* Persistent dyskinesias in patients with fetal tissue transplantation for
792 Parkinson disease. *NPJ Parkinsons Dis* **7**, (2021).

793 19. Kamath, T. *et al.* Single-cell genomic profiling of human dopamine neurons identifies a
794 population that selectively degenerates in Parkinson's disease. *Nature Neuroscience 2022*
795 *25:5* **25**, 588–595 (2022).

796 20. Siletti, K. *et al.* Transcriptomic diversity of cell types across the adult human brain.
797 *Science* **382**, eadd7046 (2023).

798 21. Mannens, C. C. A. *et al.* Chromatin accessibility during human first-trimester
799 neurodevelopment. *Nature* 1–8 (2024) doi:10.1038/s41586-024-07234-1.

800 22. Nishimura, K., Ásgrímsdóttir, E. S., Yang, S. & Arenas, E. A protocol for the
801 differentiation of human embryonic stem cells into midbrain dopaminergic neurons. *STAR*
802 *Protoc* **4**, 102355 (2023).

803 23. Sif Ásgrímsdóttir, E. *et al.* Midbrain Dopaminergic Neuron Development is Regulated by
804 Two Molecularly Distinct Subtypes of Radial Glia Cells. *bioRxiv* 2024.03.08.584031
805 (2024) doi:10.1101/2024.03.08.584031.

806 24. Desai, A. R. & McConnell, S. K. Progressive restriction in fate potential by neural
807 progenitors during cerebral cortical development. *Development* **127**, 2863–2872 (2000).

808 25. Nürnberg, E., Horschitz, S., Schloss, P. & Meyer-Lindenberg, A. Basal glucocorticoid
809 receptor activation induces proliferation and inhibits neuronal differentiation of human
810 induced pluripotent stem cell-derived neuronal precursor cells. *J Steroid Biochem Mol*
811 *Biol* **182**, 119–126 (2018).

812 26. Toledo, E. M. *et al.* Srebf1 Controls Midbrain Dopaminergic Neurogenesis. *Cell Rep* **31**,
813 107601 (2020).

814 27. Kim, W. Y. NeuroD1 is an upstream regulator of NSCL1. *Biochem Biophys Res Commun*
815 **419**, 27–31 (2012).

816 28. Murdoch, J. N., Eddleston, J., Leblond-Bourget, N., Stanier, P. & Copp, A. J. Sequence
817 and expression analysis of Nhlh1: a basic helix-loop-helix gene implicated in
818 neurogenesis. *Dev Genet* **24**, 165–177 (1999).

819 29. Dennis, D. J., Han, S. & Schuurmans, C. bHLH transcription factors in neural
820 development, disease, and reprogramming. *Brain Res* **1705**, 48–65 (2019).

821 30. Tolve, M. *et al.* The transcription factor BCL11A defines distinct subsets of midbrain
822 dopaminergic neurons. *Cell Rep* **36**, 109697 (2021).

823 31. Simon, H. H., Saueressig, H., Wurst, W., Goulding, M. D. & O'Leary, D. D. M. Fate of
824 Midbrain Dopaminergic Neurons Controlled by the Engrailed Genes. *Journal of*
825 *Neuroscience* **21**, 3126–3134 (2001).

826 32. Albéri, L., Sgadò, P. & Simon, H. H. Engrailed genes are cell-autonomously required to
827 prevent apoptosis in mesencephalic dopaminergic neurons. *Development* **131**, 3229–3236
828 (2004).

829 33. Poulin, J. F. *et al.* Mapping projections of molecularly defined dopamine neuron subtypes
830 using intersectional genetic approaches. *Nature Neuroscience 2018 21:9* **21**, 1260–1271
831 (2018).

832 34. Agoston, Z., Li, N., Haslinger, A., Wizenmann, A. & Schulte, D. Genetic and physical
833 interaction of Meis2, Pax3 and Pax7 during dorsal midbrain development. *BMC Dev Biol*
834 **12**, 10 (2012).

835 35. Nakamura, H., Katahira, T., Matsunaga, E. & Sato, T. Isthmus organizer for midbrain and
836 hindbrain development. *Brain Res Rev* **49**, 120–126 (2005).

837 36. Di Bella, D. J. *et al.* Molecular logic of cellular diversification in the mouse cerebral
838 cortex. *Nature 2021 595:7868* **595**, 554–559 (2021).

839 37. Gheldof, A., Hulpiau, P., van Roy, F., De Craene, B. & Berx, G. Evolutionary functional
840 analysis and molecular regulation of the ZEB transcription factors. *Cell Mol Life Sci* **69**,
841 2527–41 (2012).

842 38. Smidt, M. P. *et al.* Early developmental failure of substantia nigra dopamine neurons in
843 mice lacking the homeodomain gene Pitx3. *Development* **131**, 1145–1155 (2004).

844 39. Ziegler, A. B. *et al.* Cell-Autonomous Control of Neuronal Dendrite Expansion via the
845 Fatty Acid Synthesis Regulator SREBP. *Cell Rep* **21**, 3346–3353 (2017).

846 40. Yaghmaeian Salmani, B. *et al.* Transcriptomic atlas of midbrain dopamine neurons
847 uncovers differential vulnerability in a Parkinsonism lesion model. *Elife* **12**, (2024).

848 41. Storm, P. *et al.* Lineage tracing of stem cell-derived dopamine grafts in a Parkinson's
849 model reveals shared origin of all graft-derived cells. *Science Advances* **10**, 3057 (2024).

850 42. Tang, L. *et al.* A primate nigrostriatal atlas of neuronal vulnerability and resilience in a
851 model of Parkinson's disease. *Nature Communications 2023 14:1* **14**, 1–13 (2023).

852 43. Chung, S. *et al.* The homeodomain transcription factor Pitx3 facilitates differentiation of
853 mouse embryonic stem cells into AHD2-expressing dopaminergic neurons. *Molecular and*
854 *Cellular Neuroscience* **28**, 241–252 (2005).

855 44. Mesman, S., Wever, I. & Smidt, M. P. Tcf4 Is Involved in Subset Specification of
856 Mesodiencephalic Dopaminergic Neurons. *Biomedicines 2021, Vol. 9, Page 317* **9**, 317
857 (2021).

858 45. Koch, P., Opitz, T., Steinbeck, J. A., Ladewig, J. & Brüstle, O. A rosette-type, self-
859 renewing human ES cell-derived neural stem cell with potential for in vitro instruction and
860 synaptic integration. *Proc Natl Acad Sci U S A* **106**, 3225–30 (2009).

861 46. Pissadaki, E. K. & Bolam, J. P. The energy cost of action potential propagation in
862 dopamine neurons: clues to susceptibility in Parkinson's disease. *Front Comput Neurosci*
863 **7**, (2013).

864 47. del Rey, N. L. G. *et al.* Calbindin and Girk2/Aldh1a1 define resilient vs vulnerable
865 dopaminergic neurons in a primate Parkinson's disease model. *npj Parkinson's Disease*
866 *2024 10:1* **10**, 1–15 (2024).

867 48. Nie, S. *et al.* Sox6 and ALDH1A1 Truncation by Asparagine Endopeptidase Defines
868 Selective Neuronal Vulnerability in Parkinson's Disease. *Advanced Science* **12**, 2409477
869 (2025).

870 49. Pantazis, C. B. *et al.* A reference human induced pluripotent stem cell line for large-scale
871 collaborative studies. *Cell Stem Cell* **29**, 1685-1702.e22 (2022).

872 50. Zheng, G. X. Y. *et al.* Massively parallel digital transcriptional profiling of single cells.
873 *Nature Communications 2017 8:1* **8**, 1–12 (2017).

874 51. Satpathy, A. T. *et al.* Massively parallel single-cell chromatin landscapes of human
875 immune cell development and intratumoral T cell exhaustion. *Nature Biotechnology 2019*
876 *37:8* **37**, 925–936 (2019).

877 52. Korsunsky, I. *et al.* Fast, sensitive, and accurate integration of single cell data with
878 Harmony. *Nat Methods* **16**, 1289 (2019).

879 53. Stuart, T. *et al.* Comprehensive Integration of Single-Cell Data. *Cell* **177**, 1888-1902.e21
880 (2019).

881 54. Stuart, T., Srivastava, A., Madad, S., Lareau, C. A. & Satija, R. Single-cell chromatin state
882 analysis with Signac. *Nature Methods 2021 18:11* **18**, 1333–1341 (2021).

883 55. Zhang, Y. *et al.* Model-based analysis of ChIP-Seq (MACS). *Genome Biol* **9**, R137
884 (2008).

885 56. McGinnis, C. S., Murrow, L. M. & Gartner, Z. J. DoubletFinder: Doublet Detection in
886 Single-Cell RNA Sequencing Data Using Artificial Nearest Neighbors. *Cell Syst* **8**, 329-
887 337.e4 (2019).

888 57. Thibodeau, A. *et al.* AMULET: a novel read count-based method for effective multiplet
889 detection from single nucleus ATAC-seq data. *Genome Biol* **22**, 252 (2021).

890 58. Clarke, Z. A. *et al.* Tutorial: guidelines for annotating single-cell transcriptomic maps
891 using automated and manual methods. *Nature Protocols 2021 16:6* **16**, 2749–2764 (2021).

892 59. Zhou, Y. *et al.* Metascape provides a biologist-oriented resource for the analysis of
893 systems-level datasets. *Nat Commun* **10**, 1523 (2019).

894 60. Xu, C. *et al.* Automatic cell-type harmonization and integration across Human Cell Atlas
895 datasets. *Cell* **186**, 5876-5891.e20 (2023).

896 61. Domínguez Conde, C. *et al.* Cross-tissue immune cell analysis reveals tissue-specific
897 features in humans. *Science* **376**, eabl5197 (2022).

898 62. Trapnell, C. *et al.* The dynamics and regulators of cell fate decisions are revealed by
899 pseudotemporal ordering of single cells. *Nature Biotechnology 2014 32:4* **32**, 381–386
900 (2014).

901 63. Bergen, V., Lange, M., Peidli, S., Wolf, F. A. & Theis, F. J. Generalizing RNA velocity to
902 transient cell states through dynamical modeling. *Nature Biotechnology 2020 38:12* **38**,
903 1408–1414 (2020).

904 64. Gayoso, A. *et al.* Deep generative modeling of transcriptional dynamics for RNA velocity
905 analysis in single cells. *Nature Methods 2023 21:1* **21**, 50–59 (2023).

906 65. Cao, J. *et al.* The single-cell transcriptional landscape of mammalian organogenesis.
907 *Nature 2019 566:7745* **566**, 496–502 (2019).

66. Crow, M., Paul, A., Ballouz, S., Huang, Z. J. & Gillis, J. Characterizing the replicability of cell types defined by single cell RNA-sequencing data using MetaNeighbor. *Nature Communications 2018 9:1* **9**, 1–12 (2018).

67. Aibar, S. *et al.* SCENIC: Single-cell regulatory network inference and clustering. *Nat Methods* **14**, 1083–1086 (2017).

68. Faul, F., Erdfelder, E., Lang, A. G. & Buchner, A. G*Power 3: a flexible statistical power analysis program for the social, behavioral, and biomedical sciences. *Behav Res Methods* **39**, 175–191 (2007).

69. Björklund, A. & Dunnett, S. B. The Amphetamine Induced Rotation Test: A Re-Assessment of Its Use as a Tool to Monitor Motor Impairment and Functional Recovery in Rodent Models of Parkinson's Disease. *J Parkinsons Dis* **9**, 17–29 (2019).

Acknowledgements

This work was mainly supported by the European Union's Horizon 2020 (H2020) Research and Innovation Programme (Neurostemcell-Reconstruct 874758/EA) and the European Research Council (ERC) PreciseCellPD grant (Grant No. 884608/EA). Other contributors: Knut and Alice Wallenberg Foundation Wallenberg Scholar 2018.0232/EA, Vetenskaprådet VR2020-01426/EA, Chan Zuckerberg Initiative and the Silicon Valley Community Foundation (2018-191929)/EA, H2020 MSCA-ITN ASCTN/EA, H2020 Grant No. 899687 - HS-SEQ, Aligning Science Across Parkinson's (ASAP-20505)/EA, Hjärnfonden project FO2024-0195/EA. JCK and PU were supported by the German Science Foundation (516641042) and the Wenner-Gren foundation (UPD2022-0159) respectively.

The authors acknowledge support from the National Genomics Infrastructure in Stockholm funded by Science for Life Laboratory, the Knut and Alice Wallenberg Foundation and the Swedish Research Council, and NAISS/Uppsala Multidisciplinary Center for Advanced Computational Science for assistance with massively parallel sequencing and access to the UPPMAX computational infrastructure. We are grateful for the assistance of the Molecular Neurobiology

935 unit within the Department of Medical Biochemistry and Biophysics at the Karolinska Institute.
936 We would like to posthumously thank Prof. Ernest Arenas, without whom this project would not
937 have been possible.

938 Ethics declarations

939 Competing interests

940 None of the authors declare competing interests.

941 Contributions

942 R.G.S., G.L. and E.A. conceptualized the experiments. R.G.S. and G.L. redacted the manuscript.
943 R.G.S. performed *in vivo* experiments; G.L., R.K., C.S., C.T. and A.X. contributed to the *in vitro*
944 protocol development. J.C.K. contributed to the calcium imaging experiment. G.L. and A.X.
945 contributed to the *in vitro* transcriptional analysis; R.G.S. and C.A. performed the graft nuclei
946 isolation, and R.G.S. and G.L. the transcriptional analysis. C.S., G.C.B. and O.D. contributed to
947 supervision and reviewed the manuscript.